EPR Detection of $HNO_2^{\bullet-}$ in the Radiolysis of Aqueous Nitrite and Quantum Chemical Calculation of Its Stability and Hyperfine Parameters

Gordon L. Hug,*,† Donald M. Camaioni,‡ and Ian Carmichael†

Radiation Laboratory, University of Notre Dame, Notre Dame, Indiana 46556, and Pacific Northwest National Laboratories, 908 Battelle Blvd. K2-57, Richland, Washington 99352

Received: February 4, 2004; In Final Form: May 13, 2004

Experimental and theoretical evidence is presented to support a prior suggestion [Lymar et al. *J. Phys. Chem. A* **2002**, *106*, 7245] that radiolytically generated hydrogen atoms attack at the nitrogen, rather than the oxygen, of nitrite ions in aqueous solution. Time-resolved electron spin resonance detection was used to unambiguously identify the $HNO_2^{\bullet-}$ radicals formed. At pH 9 the radicals live about 10 μs, and have quite broad (0.6 G) lines. The observed hyperfine splitting at nitrogen was $a_N = 19.6$ G, with each of the three nitrogen lines further split by the small hydrogen coupling, $a_H = 4.5$ G. The *g* factor for the radical is 2.0053. Although this is the first observation of this radical in fluid solution, the ESR parameters are consistent with previous observations in the solid phase. The identity of the radical was also confirmed by quantum chemical calculation of the ESR parameters, including the *g* factor. It was necessary to take into account vibrational modulation of the computed hyperfine parameters when comparing theory to experiment because of the large-amplitude motion of the hydrogen atom in the pyramidal radical. The yield of $HNO_2^{\bullet-}$ radicals was estimated at 70% of the available H atoms by a kinetic method. Computed thermodynamic parameters confirm that, in the gas phase, both $HNO_2^{\bullet-}$ and $HONO^{\bullet-}$ are stable relative to the asymptotes $H + NO_2^-$ and $OH^- + NO$, with $HNO_2^{\bullet-}$ 40 kJ mol^{-1} above $HONO^{\bullet-}$ but protected from rearrangement by a large barrier. In solution, calculations indicate that while $HNO_2^{\bullet-}$ is still bound with respect to dissociation into $H + NO_2^-$, it is now only 3.2 kJ mol^{-1} above $HONO^{\bullet-}$ which, in turn, lies about 73 kJ mol^{-1} above $OH^- + NO$, and dissociation is driven by the strong solvation of the hydroxide ion.

Introduction

Mezyk and Bartels recently reported[1] the rate of the reaction between radiolytically generated hydrogen atoms and aqueous nitrite ions to be 1.6×10^9 dm^3 mol^{-1} s^{-1} at 25 °C. From the observed temperature dependence of the rate constant a small activation energy of around 16 kJ mol^{-1} was inferred. Partly on the basis of a limited set of molecular orbital calculations, it was assumed that H-atom addition to nitrite led directly to the products OH^- and NO, without the formation of a detectable intermediate. Only attack at oxygen was considered.

On the other hand, Lymar et al. have recently proposed[2] a novel route for the reaction of hydrogen atoms in irradiated aqueous solutions containing nitrite ions. On the basis of a reinterpretation of previous optical spectra[3] and a careful deconvolution of new spectral data, it was suggested that $HNO_2^{\bullet-}$, an adduct formed by H-atom attack at nitrogen, was present. A transient spectrum was assigned to this species, and by competitive reduction of methyl viologen, it was calculated that the entire radiolytic H-atom yield was intercepted by nitrite.

Since this reinterpretation requires a radical revision of the radiation chemistry of aqueous nitrite solutions, it is worthwhile seeking independent confirmation of the proposed mechanism. Here we report the results of a time-resolved EPR investigation into this system. We directly demonstrate the presence of the $HNO_2^{\bullet-}$ radical, estimate its formation yield, and provide a theoretical model for the observed hyperfine constants.

Some previous EPR spectra in nitrite-containing low-temperature potassium chloride crystals[4] and annealed aqueous glasses[5] have been assigned to $HNO_2^{\bullet-}$, but the species has not been previously detected in fluid solution.

In the gas phase, theoretical work has shown evidence for both O and N adducts. Van Doren et al. have discussed[6] the reaction of the hydroxide ion with nitric oxide in terms of $HONO^{\bullet-}$ (two isomers) with a long central O−N bond. In contrast to the situation in the uncharged species, the syn arrangement was slightly more stable (~1 kJ mol^{-1}) for the radical anion. Gutsev et al. reported[7] structures for HNO_2 and $HNO_2^{\bullet-}$ in the course of a coupled-cluster study on the decay channels of methyl nitrite and its anion. Sengupta et al. have determined unimolecular dissociation pathways for $HNO_2^{\bullet-}$ and characterized many stationary points on its potential energy surface from Density Functional Theory (DFT) calculations.[8] In the gas phase $HNO_2^{\bullet-}$ is computed to lie about 41 kJ mol^{-1} above $HONO^{\bullet-}$, but their interconversion is prevented by a large barrier (~177 kJ mol^{-1}). In addition $HNO_2^{\bullet-}$ lies about 40 and 113 kJ mol^{-1} below the $OH^- + NO$ and $H + NO_2^-$ dissociation limits, respectively.

Experimental Section

Materials. The chemical samples were aqueous solutions of 0.01 M sodium nitrite (Baker). The solutions were buffered with 0.01 M Borax (Fisher) and saturated with nitrous oxide. Supplementary experiments were done with sodium sulfite (Mallinckrodt) and acetylene dicarboxylic acid (Aldrich). Deionized water was used from a reverse osmosis/deionization system

* Corresponding author. E-mail: hug.1@nd.edu.
† University of Notre Dame.
‡ Pacific Northwest National Laboratories.

10.1021/jp049487e CCC: $27.50
Published on Web 07/14/2004

provided by Serv-A-Pure Co. There is an UV-irradiation unit in the circulating section of this water-purification system. The water output from the system has a resistance >18 MΩ/cm and a total organic carbon (TOC) content of <10 ppb.

Irradiation and ESR Detection. The solutions were irradiated, edge on, in a narrow 0.4 mm quartz flow cell (10 mL/min flow). The irradiation consisted of 0.5-μs pulses of 2.8 MeV electrons that are accelerated by a Van de Graaff accelerator at the Radiation Laboratory at Notre Dame. The radicals produced by the radiolysis were detected with time-resolved electron spin resonance (TRESR).[9−11] The detector signals, from a double balanced microwave mixer, are amplified appropriately, but not frequency modulated, and are finally digitized by a Biomation 8100 transient digitizer. The resulting ESR transient waveforms can be analyzed in a manner comparable to optically detected transients in pulse radiolysis.[12]

The incident electrons lose their energy in the water and produce primary radicals

$$H_2O \rightsquigarrow e_{aq}^-, {}^\bullet OH, H^\bullet, H^+ \qquad (1)$$

on the nanosecond time scale. Nitrous oxide was added to convert the hydrated electrons (e_{aq}^-) to additional hydroxyl radicals ($^\bullet$OH) by the series of reactions

$$e_{aq}^- + N_2O \rightarrow N_2 + O^{\bullet -} \qquad (2)$$

$$O^{\bullet -} + H_2O \rightarrow {}^\bullet OH + OH^- \qquad pK_a = 11.9 \qquad (3)$$

For the purpose of the calculation, the radiation chemical yields (in N_2O-saturated solutions) are taken to be $G(^\bullet OH) = 5.47$ and $G(H^\bullet) = 0.57$.[13] The radiation chemical yields are given as the number of radicals produced per 100 eV of energy deposited by the incident energy. These yields will be of interest in determining whether the yields of the newly observed radicals are produced in full or partial yield. The relative dose of the irradiation was measured by the current collected on the cell. This concentration of transients per dose (typically about 40 μM) was determined from the second-order fit to the decay of the sulfite radical $SO_3^{\bullet -}$, using $2k = 9.5 \times 10^8$ M^{-1} s^{-1}.[14] The temperature of the irradiated solution was approximately 288 K as measured by a thermocouple attached to the cell immediately on the solution's exit from the irradiated area. The solution was cooled before entry into the irradiated area and passed through a bubble trap[15] to reduce the problem of bubbles of N_2O being produced within the irradiated zone due to heating of the sample by the irradiation.

Yield Determination. The methodology of determining the yields of radicals from time-resolved TRESR has been described in some detail.[16,17] The strategy of the method is to compare the appropriately scaled amplitudes of TRESR kinetic traces from an ESR line of the radical ($R^\bullet$) with that of the single line of the sulfite radical ($SO_3^{\bullet -}$). The yield of the radical can then be determined from the relative TRESR amplitudes ($R^\bullet$ vs $SO_3^{\bullet -}$) since the $SO_3^{\bullet -}$ yield is equal to the full yield of hydroxyl radicals. Account must be taken of multiple lines and degeneracies of $R^\bullet$ in the final analysis. In principle, this method is no more sophisticated than adding up the area under the spectrum of the radical and comparing this area with the area under that of the single $SO_3^{\bullet -}$ line. However, using the modified Bloch equations[9] has the great advantage of directly accounting for saturation of the transitions, and the nonmodulated ESR detection avoids having to integrate experimental first-derivative spectra twice to obtain areas.

To execute the methodology, a series of supplementary experiments is needed to provide both instrumental parameters and the system's chemical and physical parameters for the modified Bloch equations. Both the inhomogeneous line width due to deviations from a constant magnetic field, H_0, and the magnitude of the microwave magnetic field, H_1, are estimated by using $^-O_2C-CH=C^\bullet-CO_2^-$ as the spin probe.[12] This radical is an ideal probe for these two parameters because of the long relaxation times of its electronic spin ($T_1 = 8.3$ μs and $T_2 = 6$ μs, as measured in the current work). With such long spin relaxation times, it is relatively easy to saturate the high-field transition in $^-O_2C-CH=C^\bullet-CO_2^-$ and to induce Torrey oscillations[18] in the TRESR kinetic traces. Since the period of the Torrey oscillations is very sensitive to H_1, the modified Bloch equations can be used to estimate H_1 by using literature values of T_1 and T_2 and our previous estimates[16,17] of the inhomogeneity of H_0 as first approximations in the simulations of the TRESR kinetic traces. The current value of H_1 is 0.016 G at −10 dB. This is down from earlier values[16,17] on this instrument because of the aging of the klystron, which now provides about 100 mW to the main attenuator and supplies 1.2 mW to the cavity when the main attenuator is set to −10 dB.

The long relaxation times of $^-O_2C-CH=C^\bullet-CO_2^-$ also have the effect of narrowing the lines because of the relatively small homogeneous contribution to the observed ESR line shape, and hence, long relaxation times allow a closer scrutiny of the inhomogeneous contributions to the observed line shape. To incorporate the inhomogeneity of H_0 quantitatively into the scheme, it is assumed that a Gaussian ensemble of spin systems exists and that each of these spins has an identical Lorentzian shape (characterized by T_1, T_2, and H_1) of the "slow passage" form of the original Bloch solution.[19] The Gaussian distribution represents the frequency of occurrence of such spin systems, each group of systems (characterized by i) having a local time-independent external magnetic field (H_i) different from the constant external magnetic field, H_c, at the center of the line. In this model, the observed line shape is a convolution of a Gaussian and a Lorentzian

$$f(H) = N\sum_i \left[\frac{\exp\left(-2.77\left(\frac{H_i - H_c}{W}\right)^2\right)}{\gamma_e^{\,2}(H - H_i)^2 + T_2^{\,-2} + \gamma_e^{\,2}H_1^{\,2}\frac{T_1}{T_2}} \right] \qquad (4)$$

where W is the inhomogeneity parameter and γ_e is the electron gyromagnetic ratio. W is defined to be the full-width-at-half-height of the Gaussian distribution. The line shape in eq 4 can be simulated and normalized with N to match the experimental line shape. In particular the $^-O_2C-CH=C^\bullet-CO_2^-$ high-field line shape was generated from a series of TRESR kinetic traces taken at reduced power −20 dB (to avoid saturation) and at approximately 35 μs delay following the radiolysis pulse. The line shape in eq 4 was computed for a W to match the observed line shape. H_1, determined from the Torrey oscillations, had to be reduced in accordance with the actual power setting.

The best value for W was determined to be 0.0235 G (see Figure 1a). This value is improved over our previous values[16,17] because of adjustments made to the pole pieces of the electromagnet in the interim. The value of $W = 0.0235$ is taken as characteristic for the inhomogeneity of the external constant field and was thus used for $SO_3^{\bullet -}$ and the $HNO_2^{\bullet -}$ radical also. Likewise the H_1, determined from the Torrey oscillations in the

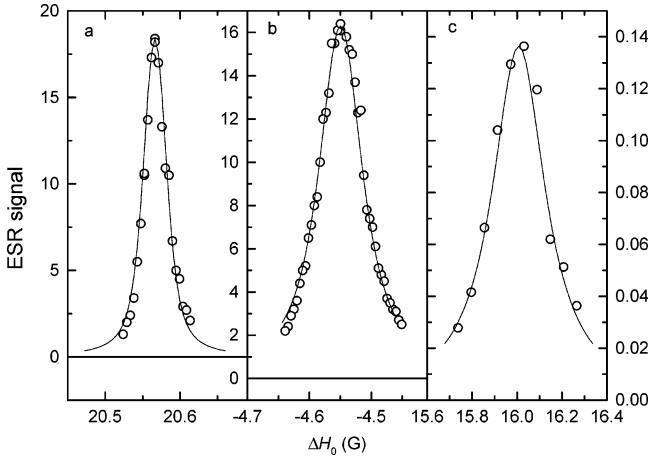

Figure 1. Line shapes of (a) $^-O_2CCH{=}{\bullet}CCO_2^-$, (b) $SO_3^{\bullet-}$, and (c) $HNO_2^{\bullet-}$. The individual points are taken from the intensity of TRESR kinetic traces at 45 to 50 μs after the radiolysis pulse for panels a and b; for panel c, the delay was only 10 μs. The simulated line shapes were generated by using eq 4 with $W = 0.0235$ G and the following parameters: (a) $H_1 = 0.005$ G, $H_c = 20.57$ G, $T_1 = 8.3$ μs, and $T_2 = 6.4$ μs; (b) $H_1 = 0.009$ G, $H_c = -4.55$ G, and $T_1 = T_2 = 1.5$ μs; and (c) $H_1 = 0.016$ G, $H_c = 16.01$ G, and $T_1 = T_2 = 0.4$ μs.

$^-O_2C-CH{=}C^{\bullet}-CO_2^-$ radical, also was used in association with these further measurements (but scaled appropriately for settings of the main attenuator). The dose and concentrations of radicals were calibrated by the concentration deduced from second-order fitting the long-time decay trace of $SO_3^{\bullet-}$ (as mentioned above, using known second-order rate constants).

These parameters are then used in the modified Bloch simulation of $SO_3^{\bullet-}$ and the radical under investigation. Before the final simulations involving the relative scaling can be done, T_1 and T_2 have to be approximated for these radicals. For radicals with relatively short spin relaxation times, T_1 is taken to be equal to T_2; some justification comes from Redfield's theory of spin relaxation times, e.g. see Chapter 5 in Slichter's book.[20] The line shape of the $SO_3^{\bullet-}$ line and the high-field line of $HNO_2^{\bullet-}$ were generated directly from kinetic traces, and T_1 and T_2 were varied in eq 4 to simulate the experimental line shapes. The line shapes of $SO_3^{\bullet-}$ and $HNO_2^{\bullet-}$ are shown in Figure 1, panels b and c, respectively, along with the simulations based on eq 4.

Collecting together all the instrumental and physical parameters, the modified Bloch equations were solved for $SO_3^{\bullet-}$ and $HNO_2^{\bullet-}$. Now the only adjustable parameters are the two corresponding scale factors, roughly analogous to the intensity of the individual line amplitudes. For the purpose of determining the scale factors, the experimental traces are taken at the center of the lines (H_c), but these traces would also have off-resonance contributions from spins that are in fields H_i characteristic of the magnetic-field inhomogeneity. To account for this in the Bloch simulations, off-resonance modified Bloch equations are solved at a representative sequence of sites characterized by the inhomogeneity parameter, W, of the same Gaussian distribution discussed above. The simulated contributions of the off-resonance spins to the central TRESR kinetic trace were normalized by their appropriate Gaussian factors.

Computational Details

Ab initio molecular orbital (MO) and DFT calculations were performed with local versions of the Aces2[21] and Gaussian98[22] suites of electronic structure programs. Preliminary DFT studies employed a modest polarized split-valence basis augmented with diffuse shells of s- and p-functions on the heavy atoms, commonly denoted 6-31+G(d,p). More thorough investigations, including characterization of relevant stationary points and a partial mapping of the intramolecular potential energy surface in $HNO_2^{\bullet-}$, used the much more flexible augmented correlation-consistent polarized valence triple-ζ basis set (aug-cc-pVTZ) of Dunning and co-workers.[23] MO-based electron correlation effects were recovered by second-order Møller−Plesset perturbation theory (MP2), quadratic configuration interaction (QCISD),[24] and coupled cluster[25] (CCSD) schemes. The highest level treatment also included (perturbatively) the effect of all connected triple replacements in the underlying Hartree−Fock determinants. Solvent effects were included by using both the CPCM[26,27] and SCIPCM[28] (parametrized for water) methods incorporated in the Gaussian series of programs. Vibrational modulation of the computed hyperfine parameters was also considered by examining the large-amplitude motion associated with out-of-plane excursions of the hydrogen. Hyperfine tensors were obtained with a contracted Gaussian basis set of better than double-ζ quality, denoted [5s2p1d,3s1p], that was previously introduced[29] for the accurate recovery of the Fermi-contact component of indirect nuclear spin−spin coupling constants in carbohydrates.

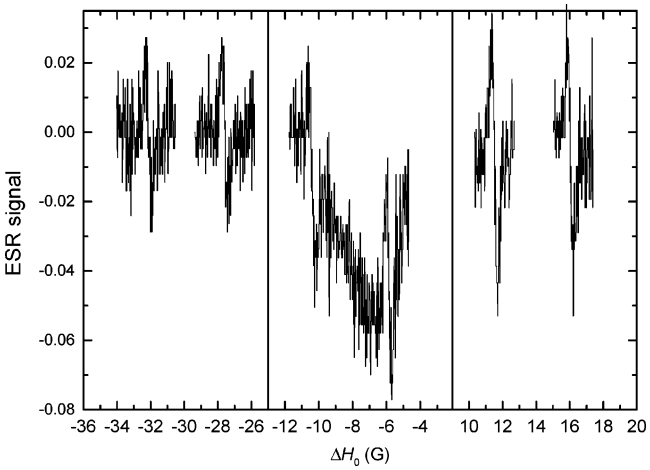

Figure 2. The TRESR spectrum of the $HNO_2^{\bullet-}$ radical taken in a time window 3.6 to 7.8 μs after the radiolysis pulse. The ESR signal was generated following the pulse radiolysis of a N_2O-saturated aqueous solution of 10 mM $NaNO_2$ and 10 mM Borax (pH 9). The magnetic field axis is offset so that zero corresponds to the radicals in quartz $g = 2.0004$.

Results and Discussion

Since the reported lifetime[2] of $HNO_2^{\bullet-}$ is relatively short and pH dependent, we chose pH 9 to search for its ESR spectrum. Figure 2 shows the TRESR spectrum of a pulse-irradiated N_2O-saturated solution of 10 mM sodium nitrite and 10 mM Borax buffer at pH 9. The time window of the observation was from 3.6 to 7.8 μs. The spectrum consists of six lines that show a small amount of chemical-induced dynamic chemical polarization (CIDEP).[30] The lines are quite broad (0.6 G from Figure 1c) and show a nitrogen hyperfine splitting of $a_N = 19.6$ G. Each of the three nitrogen lines is further split by the small hydrogen hyperfine coupling of $a_H = 4.5$ G. The g factor for the radical is 2.0053.

The $HNO_2^{\bullet-}$ radical has been identified previously by ESR techniques in solids.[4,5] In the photolysis of crystalline KCl:OH^-, CN^- at 4 K, the isotropic g(iso) = 2.0056, a_N(iso) = 21.1 G, and a_H(iso) = 1.5 G.[4] The other assignment of the $HNO_2^{\bullet-}$ radical was in a γ-irradiated powder of H_2O:HNO_2 at 77 K. In

TABLE 1: Calculated[a] Structural Parameters for $HNO_2^{\bullet-}$

	UHF	UMP2(FC)	UB3LYP	UQCISD(FC)	CCSD(T)
r_{NH}/pm	100.7	102.7	103.1	102.4	102.5
r_{NO}/pm	127.8	130.5	131.0	130.7	130.8
ϑ_{ONO}/deg	124.4	122.9	123.3	123.5	123.4
τ/deg	8.7	11.6	11.0	10.6	11.1
ΔE/kJ mol^{-1}	3.0	10.0	7.4	7.2	7.3

[a] Calculated with an aug-cc-pVTZ basis, except for CCSD(T) where the diffuse *f* was deleted from the O and N bases, and the diffuse *d* from H. τ is the deviation from planarity, and ΔE the well depth.

this latter work the isotropic parameters reported were g(iso) = 2.006 and a_N(iso) = 26.0 G. No hydrogen hyperfine coupling was reported in this work. Both of these reported isotropic g factors are consistent with the assignment of the $HNO_2^{\bullet-}$ radical in this work. The nitrogen hyperfine coupling reported by Adrian et al.[4] is also consistent with the value of 19.6 G found in the solution spectrum of the current work. The contrast of the hydrogen hyperfine coupling of 4.5 G found in the solution spectrum and the 1.5 G found in the crystalline spectrum is likely a function of the vibrational averaging that is restricted in the crystalline state. The value of 26.0 G for the powder spectrum is somewhat larger than can be rationalized, but the g factor is still consistent with the nature of the radical. Thus, overall, both the isotropic hyperfine couplings and g factors of the spectra of $HNO_2^{\bullet-}$ radicals reported in solids are consistent with an assignment of the spectrum in Figure 2 to the $HNO_2^{\bullet-}$ radical.

This assignment is strongly supported by the results of extensive quantum chemical calculations described below.

The computed structural parameters for $HNO_2^{\bullet-}$ recovered at various levels of theory are collected in Table 1. There is broad agreement among these methods indicating that the radical anion has a $^2A'$ electronic ground state and a pyramidal nuclear configuration about 10° from planarity. The planar C_{2v} structure is a transition state of $^2B_1$ electronic symmetry. The most reliable estimates place the inversion barrier at around 7 kJ mol^{-1}, thus large-amplitude motion and concomitant vibrational averaging effects are to be expected.

Similar calculations concur that the neutral HNO_2 species is planar and lies about 26 kJ mol^{-1} above the more stable nitrous acid (*anti*-)HONO arrangement. Computational estimates of the adiabatic electron affinity range from 0.31 (CCSD(T)) to 0.54 eV (B3LYP); at the UHF and UMP2 levels the anion is unbound. However, B3LYP is well-known to overestimate electron affinities, for example, at the basis set limit, it predicts a value of 3.53 eV for the electron affinity of the isolated gas-phase fluorine atom, overestimating the experimental value by 0.13 eV. We therefore prefer the lower value for HNO_2. These gas-phase results are also in accord with the ab initio predictions[7] of Gutsev et al. (r_{NH} = 103.5 pm, r_{NO} = 131.6 pm, ϑ_{ONO} =112.2°, δ_{ONHO} = 143.1°; EA = 0.30 eV) and the DFT calculations[8] of Sengupta et al. (r_{NH} = 103.1 pm, r_{NO} = 130.8 pm, ϑ_{ONO} =112.9°, δ_{ONHO} = 145.7°; EA = 0.43 eV).

The incorporation of solvent effects leads to little change in the optimized structure for the radical anion. For example, with the aug-cc-pVTZ basis set, SCIPCM calculations (0.001 au contour) predict an NH bond length of 102.3 pm, an NO bond length of 131.2 pm, and an out-of plane angle of 10.2°. On the other hand, adopting COSMO boundary conditions leads to a slight lengthening of the NH bond, to 103.3 pm with no significant change in the other parameters.

In the gas phase, at the B3LYP/aug-cc-pVTZ level of theory, the computed free energies confirm that $HNO_2^{\bullet-}$ is stable (by 90 kJ mol^{-1}) relative to the dissociation asymptote H + NO_2^-.

TABLE 2: Calculated Hyperfine Coupling Constants [G] for $HNO_2^{\bullet-}$

	gas[a]	solution[b]	exptl
$a_{iso}[^{14}N]$	23.2 (−2.4)[c]	20.8 (−2.3)[c]	19.6
$a_{iso}[^{1}H]$	16.0 (−5.8)	9.8 (−6.3)	4.5
$a_{iso}[^{17}O]$	−10.8 (+0.2)	−10.1 (+0.2)	

[a] B3LYP/[5s2p1d,3s1p]//B3LYP/aug-cc-pVTZ. [b] SCIPCM-B3LYP/[5s2p1d,3s1p]//SCIPCM-B3LYP/aug-cc-pVTZ. [c] Vibrational correction in parentheses.

While $HNO_2^{\bullet-}$ is less stable (by 44 kJ/mol at the same level) than $HONO^{\bullet-}$, a large barrier (135 kJ mol^{-1}) hinders the rearrangement by a 1,2-H atom shift. In aqueous solution calculations (cpcm model with default radii and boundary treatments) predict an increased stability (117 kJ mol^{-1}) of the HN bond in $HNO_2^{\bullet-}$, a reduced energy drop to $HONO^{\bullet-}$ (20 kJ mol^{-1}), but an increased barrier (161 kJ mol^{-1}) to intramolecular interconversion. However, in aqueous solution this transformation can be effected via protonation/deprotonation equilibria, and $HONO^{\bullet-}$ is computed, after due consideration of the important H-bonding contribution to OH^- solvation, to dissociate readily into hydroxide and NO.

Calculated DFT values for the magnetic properties are listed in Table 2. At the optimized gas-phase B3LYP/aug-cc-pVTZ geometry the computed hydrogen splitting is much larger than that observed in the present experiments (4.5 G). Averaging over the large-amplitude motion (by means of numerical integration) produces the vibrational corrections (for an effective temperature of 300 K) listed in parentheses. Reoptimizing the geometry in solution by using SCIPCM with an isodensity contour of 0.001 au also gives a substantial lowering of the computed coupling at H, and integrating over the SCIPCM potential curve finally returns an averaged value for the hyperfine splitting at H of 3.5 G at 300 K in water. At the above gas-phase geometry, UHF calculations yield a coupling at hydrogen of −6.6 G, while the UMP2 value (20.9 G) shows the usual overestimation of correlation corrections. On the other hand, with all electrons correlated, the UQCISD(T) estimate for $a(^1H)$ is 13.5 G, in reasonable accord with the B3LYP result. The computed value (at the B3LYP/aug-cc-pVTZ level) for the g-factor ranges from 2.0053 for the planar transition state to 2.0055 for the pyramidal minimum and is little changed by the presence of the solvent. These magnetic parameters are in excellent accord with the present experimental findings.

The TRESR kinetic trace, taken at the center of the high-field line at the magnetic field offset ΔH_0 = 16 G, is displayed in Figure 3. (The zero of the scale of the magnetic-field offsets is the field at which the electrons in quartz show a resonance with a corresponding g = 2.0004.) The trace of the $HNO_2^{\bullet-}$ line at 16 G shows the expected, rapid rise[1] and rapid decay[2] of the $HNO_2^{\bullet-}$ radical. The first-order decay constant used in the modified Bloch simulation shown in Figure 3 was 1.7 × 10^5 s^{-1}. The rise time of the ESR trace of $HNO_2^{\bullet-}$ was in part determined by the initial conditions, namely its rate constant for formation of the radical from hydrogen atoms of 1.62 × 10^9 M^{-1} s^{-1}.[1]

The TRESR spectrum in Figure 2 shows a modest amount of spin polarization across the entire spectrum. However, there is no noticeable polarization within the pairs of lines separated by a_H = 4.5 G. The lack of this latter type of polarization is somewhat unexpected since the spins of hydrogen atoms are normally polarized and polarization is expected to be transferred to hydrogen adducts.[12] The lack of this type of non-Boltzmann polarization indicates that the spins of the hydrogen adducts relax very fast to the Boltzmann population. Since the formation

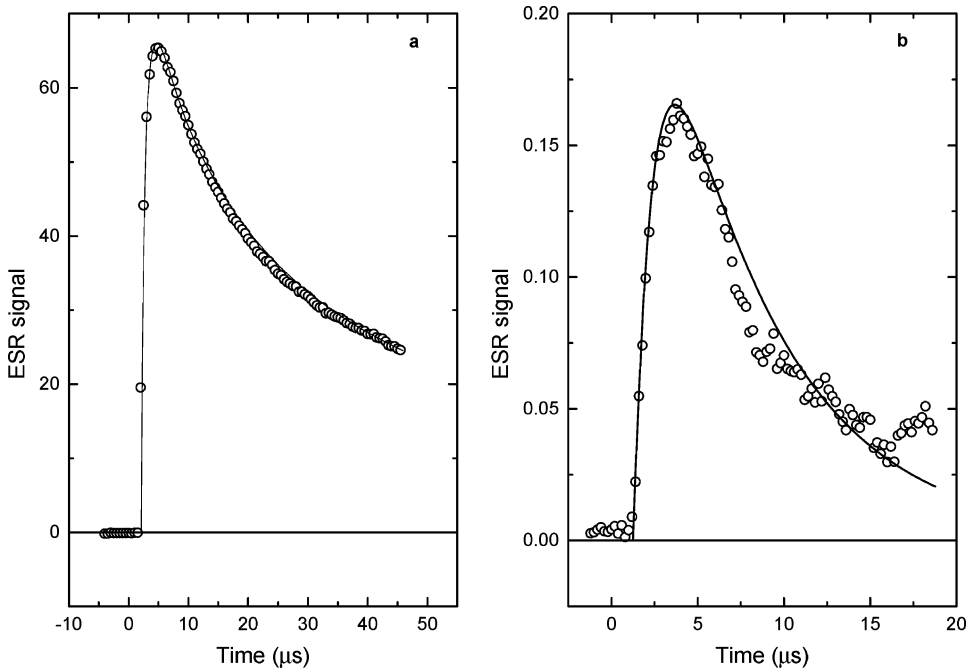

Figure 3. TRESR traces and simulations to determine the yield of radicals: (a) the reference $SO_3^{\bullet-}$, measured at the field offset of $\Delta H_0 = -4.55$ G, and (b) $HNO_2^{\bullet-}$, measured at $\Delta H_0 = 16.0$ G. The time origins of the two plots are set at the time of the radiolytic pulse; the detector is gated for the 1 to 1.5 μs during the electron pulse and immediately following.

of the adducts is so rapid,[1] the growing-in portion of the kinetic trace in Figure 3 is determined both by the RC constant (0.93 μs chosen for this radical) of the detection circuit and by the usual tipping of the magnetization by H_1. Both of these processes are specifically taken into account in the computer simulation of the adducts' formation via the modified Bloch equations.

The final computation to determine the yield of $HNO_2^{\bullet-}$ is illustrated in Figure 3. The instrumental gains were identical for the traces taken at the centers of the lines for $SO_3^{\bullet-}$ and $HNO_2^{\bullet-}$. The scale factor for $SO_3^{\bullet-}$ in Figure 3a was 4.6, and the scale factor for $HNO_2^{\bullet-}$ in Figure 3b was 0.53. However, since there are six lines of almost equal polarization, the overall scale factor for $HNO_2^{\bullet-}$ is 3.2. The kinetic trace of the highest field line ($\Delta H_0 = 16$ G) of $HNO_2^{\bullet-}$ was analyzed because it is somewhat more intense than the central and low-field lines. This means that 3.2 is the upper limit for the scale factor of $HNO_2^{\bullet-}$. The scale factor of 4.6 for $SO_3^{\bullet-}$ corresponds to the full yield of $^{\bullet}OH$ in N_2O-saturated aqueous solutions. For a full yield of radicals formed from hydrogen atoms, the scale factor should be the same, namely 4.6, since the $SO_3^{\bullet-}$ serves as the calibration of the scale factors for full yields in this methodology. Thus the scale factor for $HNO_2^{\bullet-}$ corresponds to approximately 70% of the full yield of hydrogen atoms.

This value is dependent on $G(^{\bullet}OH)$ being 5.47 in the sulfite solution and $G(^{\bullet}H)$ being 0.57 in the nitrite solution.[13] If other G values are subsequently determined, the percent yield from the ESR measurement can be recomputed simply by taking the appropriate ratios of new and old G values.

The simulated line, from the modified Bloch equations, in Figure 3b indicates a noticeable discrepancy in the tail of the decay. From other observed kinetic traces, we know that this apparent tail in the kinetic trace is only low-frequency noise as can be seen from the positive and negative deviations of the data points from the simulated line. Other unpublished data indicate that the tail of the decays goes down to the baseline as indicated in the line from the simulation.

Although the quoted yield is, in principle, an upper limit being determined from the mildly polarized high-field line, this measured yield could correspond to nearly full yield relative to hydrogen atoms, given the uncertainties involved in processing the small, noisy signals. The issue that the decay and the rise of the ESR signal of $HNO_2^{\bullet-}$ are barely an order of magnitude in difference also adds to the uncertainty of the yield. However, to the extent that the kinetic models incorporated into the modified Bloch equations are correct, this was compensated for in the kinetic simulations.

Further confirmation that hydrogen atoms were the source of the observed spectrum of $HNO_2^{\bullet-}$ was seen when the solutions were oxygen saturated before irradiation. In these solutions there was very little evidence of the spectrum shown in Figure 2. Hydrogen atoms react very rapidly ($k = 2.1 \times 10^{10}$ M^{-1} s^{-1})[31] with oxygen to form HO_2 radicals.

Conclusions

The experimental finding that the yield of $HNO_2^{\bullet-}$ radicals is equal to 70% of the radiolytic yield of H atoms indicates a clear predominance for H atom attack on the nitrogen of nitrite. The computed thermodynamic parameters confirm that $HNO_2^{\bullet-}$ is stable relative to the dissociation asymptote $H + NO_2^-$. While $HNO_2^{\bullet-}$ is less stable (by about 40 kJ mol^{-1} in solution) than $HONO^{\bullet-}$, a large barrier hinders the rearrangement by a 1,2-H atom shift. However, in aqueous solution this transformation can be effected via protonation/deprotonation equilibria, and $HONO^{\bullet-}$ is computed to dissociate readily into hydroxide and NO. This is the first reported ESR observation of $HNO_2^{\bullet-}$ radicals in fluid solution and confirms the conclusions of the optically detected pulse radiolysis work of Lymar et al.[2]

Acknowledgment. The research described herein was supported by the Environmental Management and Science Program of the U.S. Department of Energy (DOE). The Pacific Northwest National Laboratory is a multiprogram national laboratory operated by Battelle Memorial Institute for the DOE under Contract No. DE-AC06-76RLO 1830. The Notre Dame Radiation Laboratory is supported by Basic Energy Sciences of DOE.

This is Document No. NDRL-4493 from the Notre Dame Radiation Laboratory. The authors thank Professor D. Meisel for useful suggestions.

References and Notes

(1) Mezyk, S. P.; Bartels, D. M. *J. Phys. Chem.* **1997**, *101*, 6233−6237.

(2) Lymar, S. V.; Schwarz, H. A.; Czapski, G. *J. Phys. Chem. A* **2002**, *106*, 7245−7250.

(3) Grätzel, M.; Henglein, A.; Lilie, J.; Beck, G. *Ber. Bunsen-Ges.* **1969**, *73*, 646−653.

(4) Adrian, F. J.; Cochran, E. L.; Bowers, V. A. *J. Chem. Phys.* **1969**, *51*, 1018−1025.

(5) Symons, M. C. R.; Zimmerman, D. N. *J. Chem. Soc., Faraday Trans. 1* **1976**, *72*, 409−416.

(6) van Doren, J. M.; Viggiano, A. A.; Morris, R. A.; Stevens-Miller, A. E.; Miller, T. M.; Paulson, J. F.; Deakyne, C. A.; Michels, H. H.; Montgomery, J. A., Jr. *J. Chem. Phys.* **1993**, *98*, 7940−7950.

(7) Gutsev, G.; Jena, P.; Bartlett, R. J. *J. Chem. Phys.* **1999**, *110*, 403−411.

(8) Sengupta, D.; Sumathi, R.; Peyerimhoff, S. D. *Chem. Phys.* **1999**, *248*, 147−159.

(9) Verma, N. C.; Fessenden, R. W. *J. Chem. Phys.* **1976**, *65*, 2139−2155.

(10) Fessenden, R. W.; Hornak, J. P.; Venkataraman, B. *J. Chem. Phys.* **1981**, *74*, 3694−3704.

(11) Madden, K. P.; McManus, H. J. D.; Fessenden, R. W. *Rev. Sci. Instrum.* **1994**, *65*, 49−57.

(12) Fessenden, R. W. Chemically induced electron polarization of radiolytically produced radicals. In *Chemically Induced Magnetic Polarization*; Muus, L. T., Atkins, P. W., McLauchlan, K. A., Pedersen, J. B., Eds.; D. Reidel Publishing Co.: Dordrecht, Holland, 1977.

(13) Elliot, A. J.; Chenier, M. P.; Ouellette, D. C. *J. Chem. Soc., Faraday Trans.* **1993**, *89*, 1193−1197.

(14) Behar, D.; Fessenden, R. W. *J. Phys. Chem.* **1972**, *76*, 1706−1710.

(15) Duncanson, I. B. *Fusion* **1993**, *XL*, 26.

(16) Hug, G. L.; Fessenden, R. W. *J. Phys. Chem. A* **2000**, *104*, 7021−7029.

(17) Wisniowski, P.; Carmichael, I.; Fessenden, R. W.; Hug, G. L. *J. Phys. Chem. A* **2002**, *106*, 4573−4580.

(18) Torrey, H. C. *Phys. Rev.* **1949**, *76*, 1059−1068.

(19) Bloch, F. *Phys. Rev.* **1946**, *70*, 460−474.

(20) Slichter, C. P. *Principles of Magnetic Resonance*, 2nd ed.; Springer-Verlag: Berlin, Germany, 1978.

(21) Stanton, J. F.; Gauss, J.; Watts, J. D.; Nooijen, M.; Oliphant, N.; Perera, S. A.; Szalay, P. G.; Lauderdale, W. J.; Gwaltney, S. R.; Beck, S.; Balková, A.; Bernholdt, D. E.; Baeck, K.-K.; Rozyczko, P.; Sekino, H.; Hober, C.; Bartlett, R. J. ACES II, Quantum Theory Project, University of Florida, 1997.

(22) Frisch, M. J.; Trucks, G. W.; Schlegel, H. B.; Scuseria, G. E.; Robb, M. A.; Cheeseman, J. R.; Zakrzewski, V. G.; Montgomery, J. A., Jr.; Stratmann, R. E.; Burant, J. C.; Dapprich, S.; Millam, J. M.; Daniels, A. D.; Kudin, K. N.; Strain, M. C.; Farkas, O.; Tomasi, J.; Barone, V.; Cossi, M.; Cammi, R.; Mennucci, B.; Pomelli, C.; Adamo, C.; Clifford, S.; Ochterski, J.; Petersson, G. A.; Ayala, P. Y.; Cui, Q.; Morokuma, K.; Malick, D. K.; Rabuck, A. D.; Raghavachari, K.; Foresman, J. B.; Cioslowski, J.; Ortiz, J. V.; Baboul, A. G.; Stefanov, B. B.; Liu, G.; Liashenko, A.; Piskorz, P.; Komaromi, I.; Gomperts, R.; Martin, R. L.; Fox, D. J.; Keith, T.; Al-Laham, M. A.; Peng, C. Y.; Nanayakkara, A.; Gonzalez, C.; Challacombe, M.; Gill, P. M. W.; Johnson, B. G.; Chen, W.; Wong, M. W.; Andres, J. L.; Head-Gordon, M.; Replogle, E. S.; Pople, J. A. *Gaussian 98*; Gaussian, Inc.: Pittsburgh, PA, 1998.

(23) Kendall, R. A.; Dunning, T. H., Jr.; Harrison, R. J. *J. Chem. Phys.* **1992**, *96*, 6796−6806.

(24) Pople, J. A.; Head-Gordon, M.; Raghavachari, K. *J. Chem. Phys.* **1987**, *87*, 5968−5875.

(25) Purvis, G. D., III; Bartlett, R. J. *J. Chem. Phys.* **1982**, *76*, 1910−1918.

(26) Klamt, A.; Schüürmann, G. *J. Chem. Soc., Perkin Trans. 2* **1993**, 799−805.

(27) Barone, V.; Cossi, M. *J. Phys. Chem. A* **1998**, *102*, 1995−2001.

(28) Foresman, J. B.; Keith, T. A.; Wiberg, K. B.; Snoonian, J.; Frisch, M. J. *J. Phys. Chem.* **1996**, *100*, 16098−16104.

(29) Serianni, A. S.; Wu, J.; Carmichael, I. *J. Am. Chem. Soc.* **1995**, *117*, 8645−8650.

(30) *Chemical Induced Magnetic Polarization*; Muus, L. T., Atkins, P. W., McLauchlan, K. A., Pedersen, J. B., Eds.; D. Reidel: Bordrecht, Holland, 1977.

(31) Buxton, G. V.; Greenstock, C. L.; Helman, W. P.; Ross, A. B. *J. Phys. Chem. Ref. Data* **1988**, *17*, 513−886.